

Revision 1

Ab Initio Calculations of Uranium and Thorium Storage in CaSiO₃-Perovskite in the Earth's Lower Mantle

Samuel N. Perry¹, Jeffrey S. Pigott², and Wendy R. Panero^{1,*}

¹*School of Earth Sciences, Ohio State University, 274 Mendenhall Laboratory, 125 South Oval
Mall, Columbus, OH, 43210, U.S.A*

²*Department of Earth, Environmental, and Planetary Sciences, Case Western Reserve
University, Cleveland, OH, 44106, U.S.A*

*E-mail: panero.1@osu.edu

ABSTRACT

Earth's mantle convection is powered in part by the radiogenic heat released by the decay of ²³⁸U, ²³⁵U, ²³²Th and ⁴⁰K. We present ab initio calculations of uranium and thorium incorporation in CaSiO₃-perovskite with and without aluminum, and propose that aluminous calcium silicate perovskite is the likely host of uranium and thorium in the lower mantle. At 15 GPa, the enthalpies of solution into aluminum-free CaSiO₃-perovskite are 10.34 kJ/mol for U⁴⁺ and 12.52 kJ/mol for Th⁴⁺ in SiO₂ saturated systems, while the enthalpies are 17.09 kJ/mol and 19.27 kJ/mol, respectively, in CaO saturated systems. Coupled substitution of U⁴⁺ and Th⁴⁺ with aluminum is thermodynamically favored, with the enthalpies of solution negative for U⁴⁺ and near 0 kJ/mol for Th⁴⁺ throughout the stability field of CaSiO₃-perovskite. Therefore, U incorporation into CaSiO₃-perovskite is spontaneous in the presence of aluminum while Th forms a near ideal solid solution, implying these elements are potentially compatible with respect to partial melting in the transition zone and lower mantle. Further, the solid solution reactions of U⁴⁺ and Th⁴⁺ are broadly similar to each other, suggesting a restriction on the fractionation of these actinides between the upper and lower mantle. U and Th compatibility in the presence of Al has implications regarding actinide transport into the deep mantle within subducting slabs and the geochemical content of seismic anomalies at the core-mantle boundary.

30 **Keywords:** Density functional theory, calcium-silicate perovskite, lower mantle mineralogy,
31 uranium, thorium.

32 INTRODUCTION

33 Earth's heat is from two primary sources: secular cooling of the planet from primordial
34 sources and radiogenic heat dominated by the breakdown of ^{238}U , ^{235}U , ^{232}Th , and ^{40}K . Uranium
35 and thorium are the source of the majority of radiogenic mantle heat at present (Arevalo et al.,
36 2009), therefore constraining the distribution and storage of U and Th in the mantle has first-
37 order control on the heat budget of the planet.

38 Estimates of the mantle's uranium and thorium budget vary depending on the
39 compositional model used, with low estimates of 12(2)–15.4(18) ppb U and 43(4)–51.3(44) ppb
40 Th (Šrámek et al., 2013; Javoy and Kaminski, 2014) based on CI chondrites and E-chondrites
41 and consistent with mantle geoneutrino fluxes to high estimates of 20(4) ppb U and 80(12) ppb
42 Th (McDonough and Sun, 1995) estimated from peridotite melting relationships relative to
43 chondrite models for the bulk silicate earth. These differences suggest that variation in bulk
44 mantle U and Th and U/Th ratio compared to those inferred from surface melting relationships
45 may arise as a result of deep processes forming or preserving deep mantle reservoirs.

46 A consequence of uncertainty in the total U and Th budget of the mantle and the
47 distribution within the mantle is subsequent uncertainty of the fraction of the heat budget that
48 results from secular cooling versus radiogenic heating (e.g. Korenaga, 2008; Arevalo et al., 2009;
49 Javoy and Kaminski, 2014), with an impact on the interpretation of the Urey ratio, the ratio of
50 Earth's heat production to surface heat loss, an important factor in interpretation of mantle
51 dynamics. A hidden reservoir not sampled by surface volcanism is often employed to explain
52 differences between Earth's composition as determined by mantle sampling at the surface and

53 chondrite models (Korenaga, 2008). Such deep reservoirs may persist from the earliest history
54 of the planet due to fractionation of material upon solidification of a magma ocean (Labrosse et
55 al., 2007) or develop through time from present-day recycling and incomplete mixing of crustal
56 material enriched in incompatible elements (Samuel and Farnetani, 2003).

57 U and Th are incompatible in near-surface mantle melting due to their high ionic charge
58 and large ionic radius (Beattie, 1993). Because oxygen fugacity decreases with depth (Frost and
59 McCammon, 2008), U and Th are both expected to adopt the 4+ state in the deep mantle (Wood
60 et al., 1999). Of the lower mantle mineral phases, CaSiO₃-perovskite is able to accommodate
61 large cations such as U, Th and rare earth elements, with its large A-site occupied by the Ca²⁺
62 cation (Taura et al., 2001). Indeed, U and Th are compatible with CaSiO₃-perovskite (Corgne et
63 al., 2005; Corgne and Wood, 2002), in which the distribution between mineral and melt increases
64 from a peridotite to MORB bulk composition (Hirose et al., 2004). In contrast, U and Th are
65 incompatible with other lower mantle mineral phases, such as bridgmanite (MgSiO₃) and
66 ferropericlase ((Fe,Mg)O) (Corgne et al., 2005, Walter et al., 2004). Although CaSiO₃-
67 perovskite is estimated to compose no more than 8 vol% of the lower mantle (Irifune, 1994), it is
68 the main host of U and Th in the lower mantle (Corgne et al., 2005).

69 Synthesis experiments of U and Th solutions have failed to incorporate U into Al-free
70 CaSiO₃-perovskite (Gréaux et al., 2012) yet aluminous CaSiO₃-perovskite can contain up to 4
71 at% of U (Gautron et al., 2006) and up to 3.8 at% of Th (Gréaux et al., 2012). As the molar ratio
72 of Al to actinide is about 2 to 1 in these samples, this suggests a coupled substitution of 1
73 actinide defect on the Ca²⁺ A-site results in a net +2 charge on that site, referred to hereafter as
74 Act_{Ca} · in Kröger-Vink notation (Act=actinide), and 2 Al³⁺ defects on 2 Si⁴⁺ neighboring B-sites
75 generating a net -1 charge for each defect, or 2(Al_{Si}') (Gréaux et al., 2012; Gautron et al., 2006).

76 Although previous studies have proposed this substitution as the mechanism of actinide
77 incorporation in Ca-perovskite, thus far no direct simulations have been presented as supporting
78 evidence. We focus on aluminum as the most abundant minor component in CaSiO₃-perovskite
79 (e.g. Kesson et al., 1994; Kesson et al., 1996). Without such associated actinide defects, a
80 brownmillerite defect ($2\text{Al}_{\text{Si}}'+\text{V}_{\text{O}}''$) is favorable over the tschermak defect ($\text{Al}_{\text{Si}}'+\text{Al}_{\text{Ca}}'$) (Akber
81 2003), indicating the mismatch between Al^{3+} with the Ca-site. Therefore, this approach
82 considers the environment in which Al^{3+} on the Si-site is enhanced and charge compensated by
83 the effective loss of an oxygen vacancy.

84 To test this hypothesis, we present the results of ab initio calculations of U and Th oxides
85 and orthosilicates, and U and Th solid solutions of CaSiO₃-perovskite with and without Al. We
86 calculate the enthalpy of solution of the actinide species into CaSiO₃-perovskite and model the
87 dissolution of the actinides into the perovskite host over the production of minor phase oxides
88 and silicates. The result of this work informs the interpretation of the formation and preservation
89 of large-scale chemical heterogeneities in the deep mantle.

90 Additionally, uranium composes about 95% of spent nuclear fuel (Bruno and Ewing,
91 2006) and is a major part of the annually growing issue of nuclear waste disposal. Perovskite
92 (CaTiO₃) has been suggested as a component of Synroc (Ringwood, 1979) and is structurally
93 analogous to the high-pressure CaSiO₃-perovskite phase. Thus, our results may also provide
94 information on the use of perovskites in long-term actinide containment.

95 METHODS

96 We used the Vienna Ab initio Simulation Package (VASP) to relax each structure and to
97 calculate the internal energy and pressure of each phase as a function of volume. All density
98 functional theory (DFT) calculations were done using the generalized gradient approximation

99 (GGA) with the projector-augmented wave method (PAW) (Kresse and Joubert, 1999; Kresse
100 and Furthmüller, 1996). PAW potentials were employed to allow for accurate description of the
101 localized *d*- and *f*-electrons in U and Th.

102 The DFT+U method (Dudarev et al., 1998) was employed to approximate the 5*f* electrons
103 more accurately in uranium. Due to the strong electron correlation in uranium, specific care was
104 taken to avoid relaxation to metastable states (Dorado et al., 2009). The total energy is

$$105 \quad E_{DFT+U} = E_{DFT} + E_{Hub} - E_{dc} \quad (1)$$

106 where E_{DFT} is the base GGA description of the energy, E_{Hub} is the Hubbard term accounting for
107 electron-electron interaction, and E_{dc} is a double-counting correction (Dorado et al., 2009). E_{dc} is
108 described as

$$109 \quad E_{dc} = \frac{U}{2} N(N-1) - \frac{J}{2} \sum_{\sigma} N^{\sigma}(N^{\sigma}-1) \quad (2)$$

110 where U is the on-site Coulomb repulsion, J is the on-site interaction, and N is the sum of the
111 electron orbitals (Dorado et al., 2009; Liechtenstein et al., 1995). We adopt values of $U=4.50$ eV
112 and $J=0.51$ eV for uranium (Geng et al., 2007; Dudarev et al., 1997). We did not use the DFT+U
113 method for the thorium calculations, as the addition of the U energy term has been found to
114 produce a negligible effect owing to the lack of 5*f* electrons. (Song et al., 2013).

115 Enthalpy, H , is then calculated as

$$116 \quad H = E_{DFT+U} + PV \quad (3)$$

117 Where E_{DFT+U} is the internal energy as described in eqn 1, V is the volume of the
118 calculated structure, and P is pressure.

119 The crystal structures of all relevant phases were relaxed with 900 eV cutoff energy,
120 starting from their experimentally or theoretically determined unit cells and atomic positions
121 (Downs and Hall-Wallace, 2003; Wyckoff 1963; Wang et al., 2010; Taylor and Ewing, 1978;

122 Fiquet et al., 1999; Richet et al., 1988). The Monkhorst-Pack k-point meshes were 4x4x4 for the
123 actinide bearing phases, 16x16x16 for the CaO phases, 2x2x2 for CaSiO₃-perovskite and its solid
124 solutions, 8x8x8 for SiO₂ and Al₂O₃. Cutoff energies and k-point meshes were chosen so that all
125 calculations converged to within 0.02 eV per unit cell and a localization of the Th- and U-
126 bonding electrons about each atom to 5%.

127 Tetragonal CaSiO₃-perovskite (*I4/mcm*) (Shim et al., 2002; Caracas et al., 2005) and solid
128 solutions with U and Th were modeled using a 2x2x1 (79–80 atom) supercell, the minimum cell
129 size required to calculate the enthalpy of each defect (eqns 5–11). Cubic CaSiO₃-perovskite was
130 not modeled as previous diamond-anvil cell (DAC) experiments have reported CaSiO₃-
131 perovskite becoming tetragonal with the incorporation of Al and U or Th (Gréaux et al., 2012;
132 Gréaux et al., 2009; Gautron et al., 2006), a necessary consideration for modeling the
133 incorporation of actinides in the most stable configuration. Furthermore, CaSiO₃-perovskite is
134 the only lower mantle phase experimentally observed incorporating large trace element cations
135 in any substantial amount (Corgne et al., 2005). Therefore, we do not consider at this point the
136 incorporation of U and Th into bridgmanite, ferropericlase and post-perovskite, and instead focus
137 strictly on modeling the energetics of actinide incorporation into CaSiO₃-perovskite.

138 We consider two possible charge-balanced defect mechanisms: $\text{Act}_{\text{Ca}}^{\bullet\bullet} + V_{\text{Ca}}^{\bullet}$ and $\text{Act}_{\text{Ca}}^{\bullet\bullet} +$
139 $2(\text{Al}_{\text{Si}}^{\bullet})$, where V is a Ca²⁺ vacancy defect, representative brackets to the solid solution between
140 pure and highly aluminous CaSiO₃-perovskite. Alternative charge balance mechanisms were not
141 modeled as either ionic radii (Shannon and Prewitt, 1969) differed too much to be representative
142 of the lowest energy configuration (eg. $\text{Act}_{\text{Ca}}^{\bullet\bullet} + \text{Ca}_{\text{Si}}^{\bullet}$) or the substitution mechanism was not
143 realistic in context of the saturated environment we were modeling ($\text{Act}_{\text{Ca}}^{\bullet\bullet} + \frac{1}{2}V_{\text{Si}}^{\bullet\bullet\bullet}$). In the first
144 case, we assume that the $\text{Act}_{\text{Ca}}^{\bullet}$ and V_{Ca}^{\bullet} defects are on adjacent Ca sites. In the second case, we

145 assume that each Al^{3+} replaces Si^{4+} adjacent to the Act_{Ca} defect. To confirm that the defects in
146 the $2 \times 2 \times 1$ supercell (1.25 at% Act) are non-interacting due to the periodic boundary conditions
147 and that the energy we calculate can be attributed solely to each actinide defect reaction, two
148 configurations of the $2(\text{Al}_{\text{Si}}')$ were modeled in a $2 \times 2 \times 2$ supercell (160 atoms; 0.625 at% Act) at
149 the gamma point. The difference in enthalpy between the two supercell sizes is less than 15
150 J/mol, thus the $2 \times 2 \times 1$ is sufficient to describe the energy of reaction of actinide incorporation: for
151 concentrations at or below this level, the enthalpy of solution is in the dilute limit. Implicit in
152 this approach is to neglect other defects potentially active in CaSiO_3 perovskite. We address
153 these two to establish the degree to which vacancies on the Ca-site associated with the actinide
154 defect can be active.

155 We also model ThO_2 , UO_2 , ThSiO_4 , and USiO_4 to evaluate phase stability as a function of
156 pressure and for use in calculating the perovskite defect enthalpy. At high pressures, the fluorite-
157 structured ActO_2 oxides ($Fm3m$; $Z = 4$) undergo a phase change to the cotunnite-type (PbCl_2)
158 structure ($Pnma$; $Z = 4$) (Idiri et al., 2004), with some evidence for the existence of a $Pbca$ high-
159 pressure phase of the ActO_2 oxides (Gréaux et al., 2008). The actinide silicates are isostructural
160 with zircon (ZrSiO_4) ($I4_1/amd$; $Z = 4$) at ambient pressure, but do not undergo the same
161 transitions at high pressure. USiO_4 becomes isostructural to the scheelite structure ($I4_1/a$; $Z = 4$)
162 (Bauer et al., 2014; Zhang et al., 2009) and ThSiO_4 transforms to huttonite, a monazite-
163 structured phase ($P2_1/n$; $Z = 4$) (Bose et al., 2009).

164 The stability of the silicates relative to the oxides was determined

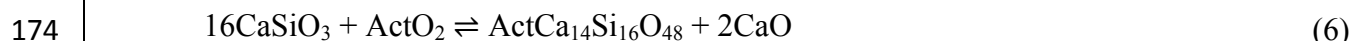
165 by $\text{ActSiO}_4 \rightleftharpoons \text{ActO}_2 + \text{SiO}_2$ (4)

166 in which SiO_2 is calculated as stishovite below 45 GPa and the CaCl_2 -structured phase above.

167 The dominance of the $\text{Act}_{\text{Ca}}^{\bullet\bullet} + V_{\text{Ca}}^{\prime\prime}$ relative to the $\text{Act}_{\text{Ca}}^{\bullet\bullet} + 2(\text{Al}_{\text{Si}}^{\prime})$ defect is established
168 by comparing the enthalpies of reaction

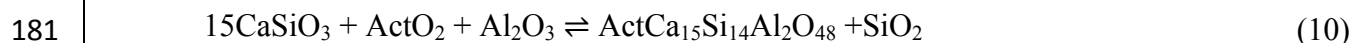


170 The enthalpy of formation in CaSiO_3 -perovskite is a function of the stability of the pure
171 actinide phase, and therefore dependent upon the breakdown of the silicate, ActSiO_4 to its oxides
172 $\text{ActO}_2 + \text{SiO}_2$, and further a function of the relative saturation of the system with respect to CaO
173 or SiO_2 . The formation of the $\text{Act}_{\text{Ca}}^{\bullet\bullet} + V_{\text{Ca}}^{\prime\prime}$ defect is determined by the relevant reaction,



178 in which equations (6) and (8) are relevant to CaO saturated systems and equations (7) and (9)
179 are relevant to SiO_2 saturated systems.

180 Analogously, the formation of the $\text{Act}_{\text{Ca}}^{\bullet\bullet} + 2(\text{Al}_{\text{Si}}^{\prime})$ defect is calculated by



183 depending upon the relative stability of equation 4.

184 RESULTS

185 [Table 1]

186 We confirm the transition of the fluorite-structured ActO_2 oxides to the high-pressure
187 *Pnma* phase (Fig. 1; Table 1), and find that the suggested *Pbca* phase (Gréaux et al., 2008) is not
188 stable at any pressure for either actinide oxide. ThO_2 will undergo the *Fm3m* to *Pnma* phase
189 transition at 26.9 GPa and UO_2 will experience the same structural transition at 29.2 GPa. At

190 pressures exceeding ~80 GPa the *Pnma* phase of ThO₂ experiences a structural collapse of the *a*-
191 axis, associated with an expansion of the *b*- and *c*-axis, likely comparable to the ZrO₂ post-
192 cotunnite phase change to Fe₂P structure (Nishio-Hamane et al., 2015). As we expect a similar
193 phase change for UO₂, we therefore limit our results to below 80 GPa. We further confirm the
194 transition of the ActSiO₄ silicates to the high-pressure phases of huttonite for ThSiO₄ and
195 scheelite (CaWO₄) structure for USiO₄ (Fig. 1) at 5.1 and 6.4 GPa, respectively.

196 [Figure 1]

197 ThSiO₄-huttonite is stable relative to the oxides to 11.1 GPa, above which ThO₂ + SiO₂ is
198 the stable assemblage. In contrast, scheelite-structured USiO₄ is stable relative to oxides to 51.7
199 GPa (Fig. 2; Table 1). This pressure difference of the breakdown to the oxides represents a
200 potential difference in geochemical behavior of Th and U phases in the transition zone and upper
201 portion of the lower mantle.

202 [Figure 2]

203 The Act_{Ca}^{••} + V_{Ca}^{''} defect in CaSiO₃-perovskite is most stable for the calcium vacancy as
204 nearest neighbor to the Act_{Ca}^{••} defect, with little difference in the direction, reflecting the slight
205 tetragonal splitting of the nominal cubic structure. The vacancy compensated U and Th defects
206 expand the unit cell by 0.15% and 0.26%, respectively, at 15 GPa and remains nearly constant
207 over the pressure range of the calculations. The coupled Act_a^{••} + 2(Al_{Si}') defect is also most
208 stable when the defects are clustered together. The enthalpy of the Al_{Si}' defects when placed
209 on opposite sides of the Act_{Ca}^{••} defect in the (011) direction (Fig. 3) are within 0.2% of the Al_{Si}'
210 defects oriented in the (001) direction. The defects appear to be non-interacting at this
211 concentration, in which the defect enthalpies are negligibly lower than in the 2x2x1 supercell
212 calculation. The aluminum compensated U and Th defects expand the unit cell significantly

213 more than the vacancy compensated lattice, with a 2.5% and 2.2% volume expansion at 15 GPa,
214 respectively. As with the vacancy compensated defects, the expansion of the lattice is
215 approximately constant over the pressure range of the calculations.

216 [Figure 3]

217 The $\text{Act}_{\text{Ca}^{2+}} + 2(\text{Al}_{\text{Si}^{\prime}})$ defect is more stable than the $\text{Act}_{\text{Ca}^{2+}} + V_{\text{Ca}^{2+}}$ defect (eqn 4; Fig. 4),
218 suggesting that the presence of Al^{3+} in the system plays a critical role in actinide compatibility
219 into the perovskite host. The $\text{Th}_{\text{Ca}^{2+}} + 2(\text{Al}_{\text{Si}^{\prime}})$ defect is 11 kJ/mol more stable than the $\text{Th}_{\text{Ca}^{2+}} +$
220 $V_{\text{Ca}^{2+}}$ defect at ambient pressure, increasing to 30 kJ/mol more stable at 80 GPa. In contrast, the
221 $\text{U}_{\text{Ca}^{2+}} + 2(\text{Al}_{\text{Si}^{\prime}})$ defect is 30–40 kJ/mol more stable than the $\text{U}_{\text{Ca}^{2+}} + V_{\text{Ca}^{2+}}$ defect, approximately
222 constant throughout the 0-80 GPa range of the calculations.

223 [Figure 4]

224 Calculation of the formation enthalpies of the $\text{Act}_{\text{Ca}^{2+}} + V_{\text{Ca}^{2+}}$ (eqns 6 – 9) and $\text{Act}_{\text{Ca}^{2+}} +$
225 $2(\text{Al}_{\text{Si}^{\prime}})$ (eqns 10 – 11) defects, we find the $\text{U}_{\text{Ca}^{2+}} + 2(\text{Al}_{\text{Si}^{\prime}})$ defect is negative at all pressures up
226 to at least 80 GPa, varying between -28 and -9.5 kJ/mol over the pressure range of the
227 calculations, while the $\text{Th}_{\text{Ca}^{2+}} + 2(\text{Al}_{\text{Si}^{\prime}})$ defect is <0.5 kJ/mol above 11 GPa (Fig. 5). Conversely,
228 the vacancy compensated defect has a positive enthalpy that increases with pressure, in which
229 the solution enthalpy of U^{4+} incorporation is between 9 and 14 kJ/mol for all pressures in SiO_2 -
230 saturated systems, and increases from 14 to 32 kJ/mol from 0 to 80 GPa in CaO-saturated
231 systems. The behavior of Th^{4+} is similar in which reaction enthalpy for the formation of the
232 defect is between 12 and 21 kJ/mol when SiO_2 -saturated, and increases from 16 to 39 kJ/mol
233 when CaO saturated (Fig. 5).

234 [Figure 5]

235

DISCUSSION

236 | Calculated structures and compressibilities of ActO_2 oxides and ActSiO_4 silicates are
237 | broadly consistent with experiment and prior ab initio calculations (Table 1). Differences
238 | between our equations of state and previously published calculations are a function of the cutoff
239 | energy. We can reproduce the softer equations of state by reducing the cutoff energy to 500 eV,
240 | but choose the higher cutoff energy (900 eV) to retain precision in the relative energies between
241 | phases to high pressure. All calculations tend to predict a lower pressure of transition relative to
242 | the experimentally suggested values, which are all based on room temperature diamond-anvil
243 | cell experiments. At room temperature, these measurements can be subject to kinetic barriers or
244 | non-hydrostatic stresses (Klotz et al., 2009), which may also explain the differences between
245 | calculated and measured results.

246 | Although a low-temperature transition of ThSiO_4 from the zircon structure to the
247 | scheelite structure has been suggested (Bose et al., 2009), our calculations instead confirm a
248 | transition from thorite to huttonite (Liu, 1982) at approximately 5.1 GPa. We calculate the
249 | transition of USiO_4 from coffinite (zircon structure) to the scheelite structure at 6.4 GPa, which
250 | is lower than the reported 14 – 17 GPa of previous studies (Bauer et al., 2014; Zhang et al.,
251 | 2009). The contrast between these and previous computational results appear to reside in the
252 | cutoff energy (here 900 eV compared to 610 eV in Bauer et al., 2014) and potentially from the
253 | treatment of the Hubbard energy (here 4.5 eV versus 2 eV in Bauer et al., 2014). Too soft a
254 | cutoff energy will tend to fail to localize the f -electrons about the actinide element.

255 | In the $\text{ActO}_2\text{-CaO-SiO}_2\text{-Al}_2\text{O}_3$ system, defect enthalpy decreases with SiO_2 saturation,
256 | and becomes spontaneous to the extent that CaSiO_3 -perovskite forms with minor Al_2O_3 (Fig. 5).
257 | Mantle pyrolite and basalt assemblages show that the distribution of Al_2O_3 between CaSiO_3 -
258 | perovskite and bridgmanite significantly favors the bridgmanite phase, with a partition

259 coefficient, D_{Ca-Pv/Br_2}^{Al} of $\sim 0.1-0.2$ over the pressure and temperature range of the lower mantle
260 (Nishio-Hamane et al., 2007). Therefore for a mantle with ~ 4 wt% Al_2O_3 , this suggests ~ 0.5
261 wt% Al_2O_3 in the calcium phase, consistent with measurements in pyrolitic and basaltic
262 compositions to the core mantle boundary (e.g. Kesson et al., 1994; Kesson et al., 1998). Our
263 results suggest incorporation of U^{4+} and Th^{4+} is more favorable in an environment with excess Si
264 and Al. Even in the presence of aluminum, while the reaction enthalpy with Th^{4+} is nearly ideal,
265 U^{4+} reactions are more negative throughout the stability field of $CaSiO_3$ -perovskite (Fig. 5), with
266 the defect enthalpy of U^{4+} 18 kJ/mol lower than Th^{4+} at 15 GPa and 10 kJ/mol at 80 GPa.
267 However, the U^{4+} and Th^{4+} coupled substitutions are broadly similar, implying similar
268 incorporation behavior into the perovskite host.

269 IMPLICATIONS

270 Melt-crystal partitioning measurements of U and Th in $CaSiO_3$ -perovskite are made at
271 relatively low pressures (Taura et al., 2001; Corgne and Wood, 2002; Hirose et al., 2004; Corgne
272 et al., 2005), yet equilibration in a deep magma ocean potentially occurs at significantly greater
273 pressure than those employed in these experiments, potentially as deep as the base of the mantle
274 (Labrosse et al., 2007). The reaction enthalpy of U and Th with aluminous $CaSiO_3$ -perovskite is
275 roughly constant in the solid state between 0 and 80 GPa. As the melt structure changes slowly
276 under the conditions of the lower mantle (de Koker et al., 2008), this suggests that the
277 melt/mineral partitioning is likely to remain compatible and applicable through the lower
278 mantle. However, the static calculations presented here exclude direct consideration of
279 configurational and vibrational entropy from the defect reactions. However, as the defects are
280 the same between the two systems, the configurational entropic contributions will be identical
281 for Th and U incorporation in $CaSiO_3$ -perovskite, and the vibrational effects should be
minimally different

282 from Th- and U-free perovskites for trace concentrations. The effects of configurational entropy,
283 S_{config} , will be to stabilize the Gibbs free energy of the defect reaction, G_{rxn} , through $G_{rxn} = H_{rxn} -$
284 TS_{config} in equal proportions for U and Th, and therefore the conclusions are unchanged.
285 Furthermore, these results clarify the effect of actinide incorporation in $CaSiO_3$ with excess
286 alumina: The increase in Al-defects will enhance the dissolution of the actinide through
287 additional possible configurations. Therefore, the concentration-dependent defect population will
288 be driven not by the actinide concentration but by the alumina concentration. We cannot,
289 however, exclude the possibility of further phase changes in UO_2 and ThO_2 at pressures in excess
290 of 80 GPa that would change their behavior. As these are reference phases in determining the
291 enthalpies of reaction, any first-order phase transitions will affect the solubility of U and Th into
292 $CaSiO_3$ -perovskite.

293 Subducting slabs are saturated in SiO_2 -stishovite below 300 km and enriched in
294 aluminous phases (Irifune and Ringwood, 1993), such that $CaSiO_3$ -perovskite forms in
295 environments mostly likely to dissolve U^{4+} and Th^{4+} . Deeply subducted oceanic lithosphere
296 hosting $CaSiO_3$ -perovskite is therefore a likely phase for transporting U and Th into the lower
297 mantle through retention of actinides already present in enriched continental sediments.
298 Remnants of ancient slabs enriched in heat producing elements near the core mantle boundary
299 (CMB) could potentially be a geochemical source of large low-shear-wave velocity provinces
300 (LLSVPs) beneath Africa and the Pacific, enriched in heat producing elements through
301 sequestration of crustal material (White, 2015). Furthermore, these results imply that the
302 LLSVPs could have formed due to preferential U and Th incorporation into $CaSiO_3$ -perovskite
303 via fractional crystallization as a basal magma ocean solidified (Labrosse et al., 2007).

- 327 Beattie, P. (1993) Uranium–thorium disequilibria and partitioning on melting of garnet
328 peridotite. *Nature*, 363, 63-65.
- 329 Bose, P.P., Mittal, R., and Chaplot, S.L. (2009) Lattice dynamics and high pressure phase
330 stability of zircon structured natural silicates. *Physical Review B*, 79,
331 174301. [Bruno, J. and Ewing, R.C. \(2006\) Spent nuclear fuel. *Elements*, 2, 343-349.](#)
- 332 [Caracas, R., Wentzcovitch, R., Price, G.D., and Brodholt, J. \(2005\). *CaSiO₃* perovskite at lower](#)
333 [mantle pressures. *Geophysical Research Letters*, 32, L06306.](#)
- 334 Corgne, A., and Wood, B.J. (2002) *CaSiO₃* and *CaTiO₃* perovskite melt partitioning of
335 trace elements: Implications for gross mantle differentiation. *Geophysical Research Letters*, 29,
336 DOI:10.1029/2001GL014398.
- 337 [Corgne, A., Allan, N.L., and Wood, B.J. \(2003\). Atomistic simulations of trace element](#)
338 [incorporation into the large site of *MgSiO₃* and *CaSiO₃* perovskites. *Physics of the Earth*](#)
339 [and Planetary Interiors](#), 139, 113-127.
- 340 Corgne, A., Liebske, C., Wood, B.J., Rubie, D.C., and Frost, D.J. (2005) Silicate perovskite-melt
341 partitioning of trace elements and geochemical signature of a deep perovskite reservoir.
342 *Geochimica et Cosmochimica Acta*, 69, 485-496.
- 343 [de Koker, N.P., Stixrude, L., and Karki, B.B. \(2008\). Thermodynamics, structure, dynamics, and](#)
344 [freezing of *Mg₂SiO₄* liquid at high pressure. *Geochimica et Cosmochimica Acta*, 72,](#)
345 [1427-1441.](#)
- 346 Dorado, B., Amadon, B., Freyss, M., and Bertolus, M. (2009) DFT+U calculations of the ground
347 state and metastable states of uranium dioxide. *Physical Review B – Condensed*
348 *Matter and Materials Physics*, 79, 235125.

- 349 Downs, R.T., and Hall-Wallace, M. (2003) The American Mineralogist crystal structure
350 database. American Mineralogist, 88, 247-250.
- 351 Dudarev, S.L., Manh, D.N. and Sutton, A.P. (1997) Effect of Mott-Hubbard correlations on the
352 electronic structure and structural stability of uranium dioxide. Philosophical Magazine B,
353 75, 613-628.
- 354 Dudarev, S.L., Botton, G.A., Savrasov, S.Y., Humphreys, C.J., and Sutton, A.P. (1998) Electron-
355 energy-loss spectra and the structural stability of nickel oxide: An LSDA+U study.
356 Physical Review B, 57, 1505-1509.
- 357 Fiquet, G., Richet, P., and Montagnac, G. (1999) High-temperature thermal expansion of lime,
358 periclase, corundum and spinel. Physics and Chemistry of Minerals, 27, 103-111.
- 359 Fonseca, R.O.C., Mallmann, G., Sprung, P., Sommer, J.E., Heuser, A., Speelmanns, I.M., and
360 Blanchard, H. (2014) Redox controls on tungsten and uranium crystal/silicate melt
361 partitioning and implications for the U/W and Th/W ratio of the lunar mantle. Earth
362 and Planetary Science Letters, 404, 1-13.
- 363 Frost, D.J., and McCammon, C.A. (2008) The redox state of Earth's mantle. Annual Review
364 Earth and Planetary Science, 36, 389-420.
- 365 Gautron, L., Greaux, S., Andrault, D., Bolfan-Casanova, N., Guignot, N., and Bouhifd, M.A.
366 (2006) Uranium in the Earth's lower mantle. Geophysical Research Letters, 33, L23301,
367 DOI: 10.1029/2006GL027508.
- 368 Geng, H.Y., Chen, Y., Kaneta, Y., and Kinoshita, M. (2007) Structural behavior of uranium
369 dioxide under pressure by LSDA+U calculations. Physical Review B, 75, 054111.

- 370 Gréaux, S., Farges, F., Gautron, L., Trcera, N., Flank, A., and Lagarde, P. (2012) X-ray
371 absorption near edge structure (XANES) study of the speciation of uranium and thorium
372 in Al-rich CaSiO₃ perovskite. *American Mineralogist*, 97, 100-109.
- 373 Gréaux, S., Gautron, L., Andrault, D., Bolfan-Casanova, N., Guignot, N., and Bouhifd, M.A.
374 (2009) Experimental high pressure and high temperature study of the incorporation of
375 uranium in Al-rich CaSiO₃ perovskite. *Physics of the Earth and Planetary Interiors*, 174,
376 254-263.
- 377 Gréaux, S., Gautron, L., Andrault, D., Bolfan-Casanova, N., Guignot, N., and Haines, J. (2008)
378 Structural characterization of natural UO₂ at pressures up to 82 GPa and temperatures up
379 to 2200 K. *American Mineralogist*, 93, 1090-1098.
- 380 Hirose, K., Shimizu, N., van Westrenen, W., and Fei, Y. (2004) Trace element partitioning in
381 Earth's lower mantle and implications for geochemical consequences of partial melting at
382 the core-mantle boundary. *Physics of the Earth and Planetary Interiors*, 146, 249-260.
- 383 Idiri, M., Le Bihan, T., Heathman, S., and Rebizant, J. (2004) Behavior of actinide dioxides
384 under pressure: UO₂ and ThO₂. *Physical Review B*, 70, 014113.
- 385 Irifune, T., and Ringwood, A.E. (1993) Phase transformations in subducted oceanic crust and
386 buoyancy relationships at depths of 600–800 km in the mantle. *Earth and Planetary
387 Science Letters*, 117, 101-110. Javoy, M., and Kaminski, E. (2014) Earth's Uranium and
388 Thorium content and geoneutrinos fluxes based on enstatite chondrites. *Earth and
389 Planetary Science Letters*, 407, 1-8.
- 390 Irifune, T. (1994) Absence of an aluminous phase in the upper part of the Earth's lower mantle.
391 *Nature*, 370, 131-133.

- 392 Kesson, S.E., Gerald, J.F., and Shelley, J.M. (1998). Mineralogy and dynamics of a pyrolite
393 lower mantle. *Nature*, 393, 252-255.
- 394 Kesson, S.E., Gerald, J.F., and Shelley, J.M.G. (1994). Mineral chemistry and density of
395 subducted basaltic crust at lower-mantle pressures. *Nature*, 372, 767-769.
- 396 Klotz, S., Chervin, J-C., Munsch, P., and Le Marchand, G. (2009) Hydrostatic limits of 11
397 pressure transmitting media. *Journal of Physics D Applied Physics*, 42, 075413.
- 398 Korenaga, J. (2008) Urey ratio and the structure and evolution of Earth's mantle. *Reviews of*
399 *Geophysics*, 46, RG2007, DOI:10.1029/2007RG000241.
- 400 Kresse, G., and Joubert, D. (1999) From ultrasoft pseudopotentials to the projector augmented-
401 wave method. *Physical Review B*, 59, 1758-1775.
- 402 Kresse, G., and Furthmüller, J. (1996) Efficient iterative schemes for ab initio total-energy
403 calculations using a plane-wave basis set. *Physical Review B*, 6, 15-50.
- 404 Labrosse, S., Hernlund, J., and Coltice, N. (2007) A crystallizing dense magma ocean at the base
405 of the Earth's mantle. *Nature*, 450, 866-869.
- 406 Liechtenstein, A., Anisimov, V., and Zaanen, J. (1995) Density-functional theory and strong
407 interactions: Orbital ordering in Mott-Hubbard insulators. *Physical Review B*, 52, R5467-
408 R5470.
- 409 Liu, L. (1982) Phase transformations in MSiO_4 compounds at high pressures and their
410 geophysical implications. *Earth and Planetary Science Letters*, 57, 110-116.
- 411 McDonough, W.F., and Sun, S. (1995) The composition of the Earth. *Chemical Geology*, 120,
412 223-253.

- 413 Nishio-Hamane, D., Dekura, H., Seto, Y., and Yagi, T. (2015) Theoretical and experimental
414 evidence for the post-cotunnite phase transition in zirconia at high pressure. *Physics and*
415 *Chemistry of Minerals*, 42, 385-392.
- 416 Nishio-Hamane, D., Seto, Y., Nagai, T., and Fujino, K. (2007) Ferric iron and aluminum
417 partitioning between MgSiO₃- and CaSiO₃-perovskites under oxidizing conditions. *Journal*
418 *of Mineralogical and Petrological Sciences*, 102, 291-297.
- 419 Qiang, L., Jun-Sheng, Y., Duo-Hui, H., Qi-Long, C., and Fan-Hou, W. (2014) Phase transition
420 and thermodynamic properties of ThO₂: Quasi-harmonic approximation calculations and
421 anharmonic effects. *Chinese Physics B*, 23, 017101.
- 422 Richet, P., Mao, H., and Bell, P.M. (1988) Static compression and equation of state of CaO to
423 1.35 Mbar. *Journal of Geophysical Research: Solid Earth*, 93, 15279-15288.
- 424 Ringwood, A.E., Kesson, S.E., Ware, N.G., Hibberson, W., and Major, A. (1979) Immobilisation
425 of high level nuclear reactor wastes in SYNROC. *Nature*, 278, 219-223.
- 426 Samuel, H., and Farnetani, C.G. (2003) Thermochemical convection and helium concentrations
427 in mantle plumes. *Earth and Planetary Science Letters*, 207, 39-56.
- 428 Shannon, R.D. and Prewitt, C.T. (1969) Effective ionic radii in oxides and fluorides. *Acta*
429 *crystallographica*, B25, 925-946.
- 430 Shim, S.H., Jeanloz, R., & Duffy, T.S. (2002). Tetragonal structure of CaSiO₃ perovskite above
431 20 GPa. *Geophysical Research Letters*, 29, 2166.
- 432 Siebert, J., Badro, J., Antonangeli, D. and Ryerson, F.J. (2012) Metal–silicate partitioning of Ni
433 and Co in a deep magma ocean. *Earth and Planetary Science Letters*, 321, 189-197.

- 434 Song, H.X., Liu, L., Geng, H.Y. and Wu, Q. (2013) First-principle study on structural and
435 electronic properties of CeO₂ and ThO₂ under high pressures. *Physical Review B*, 87,
436 184103.
- 437 Šrámek, O., McDonough, W.F., Kite, E.S., Lekić, V., Dye, S.T., and Zhong, S. (2013)
438 Geophysical and geochemical constraints on geoneutrino fluxes from Earth's mantle.
439 *Earth and Planetary Science Letters*, 361, 356-366.
- 440 Taura, H., Yurimoto, H., Kato, T., and Sueno, S. (2001) Trace element partitioning between
441 silicate perovskites and ultracalcic melt. *Physics of the Earth and Planetary Interiors*, 124,
442 25-32.
- 443 Taylor, M., and Ewing, R.C. (1978) The crystal structures of the ThSiO₄ polymorphs: huttonite
444 and thorite. *Acta Crystallographica Section B: Structural Crystallography and Crystal*
445 *Chemistry*, 34, 1074-1079.
- 446 Walter, M.J., Nakamura, E., Trønnes, R.G. and Frost, D.J. (2004) Experimental constraints on
447 crystallization differentiation in a deep magma ocean. *Geochimica et Cosmochimica Acta*,
448 68, 4267-4284.
- 449 Wang, B., Shi, H., Li, W., and Zhang, P. (2010) First-principles study of ground-state properties
450 and high pressure behavior of ThO₂. *Journal of Nuclear Materials*, 399, 181-188.
- 451 White, W.M. (2015) Isotopes, DUPAL, LLSVPs, and Anekantavada. *Chemical Geology*, 419,
452 10-28.
- 453 Wood, B.J., Blundy, J.D., and Robinson, J.A.C. (1999) The role of clinopyroxene in generating
454 U-series disequilibrium during mantle melting. *Geochimica et Cosmochimica Acta*, 63,
455 1613-1620.

- 456 Wyckoff, R. (1963) Structures of the Compounds RX_2 . In Crystal Structures 1, 2nd ed., p. 239-
457 243. Interscience Publishers, New York, New York.
- 458 Zhang, F.X., Pointeau, V., Shuller, L.C., Reaman, D.M., Lang, M., Liu, Z., Hu, J., Panero, W.R.,
459 Becker, U., Poinssot, C., and Ewing, R.C. (2009) Structural transitions and electron
460 transfer in coffinite, $USiO_4$, at high pressure. American Mineralogist, 94, 916-920.
461

462

FIGURE CAPTIONS

463 **Figure 1.** Pressure induced phase transitions in ActSiO_4 ($\text{Act} = \text{Th}$, blue; $\text{Act} = \text{U}$, red) zircon
464 structure to monazite and scheelite structures (dash dot), in ActO_2 $Fm3m$ to $Pnma$ (solid), and
465 the disfavored $Pbca$ phase (dash).

466 **Figure 2.** The breakdown of ActSiO_4 ($\text{Act} = \text{Th}$, blue; $\text{Act} = \text{U}$, red) to the binary oxides ActO_2
467 + SiO_2 (stishovite). Huttonite (ThSiO_4) decomposes to oxides at 11.1 GPa, scheelite-structure
468 USiO_4 persists to lower mantle pressures and breaks down at approximately 51.7 GPa. **Figure**

469 **3.** The structures of CaSiO_3 -perovskite with $\text{Act}_{\text{Ca}}^{\bullet\bullet} + V_{\text{Ca}}^{\bullet}$ defects (left) and $\text{Act}_{\text{Ca}}^{\bullet\bullet}$ and
470 $2(\text{Al}_{\text{Si}}')$ defects (right): blue octahedra are SiO_6 units, light blue octahedra are $\text{Al}_{\text{Si}}\text{O}_6$, blue-gray
471 sphere are Ca^{2+} atoms, and the green sphere is the $\text{Act}_{\text{Ca}}^{\bullet\bullet}$ defect.

472 **Figure 4.** The exchange between the $\text{Act}_{\text{Ca}}^{\bullet\bullet} + V_{\text{Ca}}^{\bullet}$ and $\text{Act}_{\text{Ca}}^{\bullet\bullet} + 2(\text{Al}_{\text{Si}}')$ defects according to
473 equation 4 ($\text{Act} = \text{Th}$, blue; $\text{Act} = \text{U}$, red)

474 **Figure 5.** The enthalpy (H) of defect formation for the $\text{Act}_{\text{Ca}}^{\bullet\bullet} + 2(\text{Al}_{\text{Si}}')$ and $\text{Act}_{\text{Ca}}^{\bullet\bullet} +$
475 V_{Ca}^{\bullet} reactions ($\text{Act} = \text{Th}$, blue; $\text{Act} = \text{U}$, red). Phase transformations in the oxides and silicates
476 are marked according to a = ThSiO_4 ($I4_1/amd$) to ThSiO_4 ($P2_1/n$), b = USiO_4 ($I4_1/amd$) to USiO_4
477 ($I4_1/a$), c = ThSiO_4 ($P2_1/n$) to ThO_2 ($Fm3m$) + SiO_2 , d = ThO_2 ($Fm3m$) to ThO_2 ($Pnma$), e =
478 USiO_4 ($I4_1/a$) to UO_2 ($Pnma$) + SiO_2 , f = CaO (B1) to CaO (B2).

Parameter	ThO ₂ (<i>Fm3m</i>)		ThO ₂ (<i>Pnma</i>)		ThSiO ₄ (<i>I4₁/amd</i>)		ThSiO ₄ (<i>P2₁/n</i>)	
	Thorianite		—		Thorite		Huttonite	
	Theory	Experiment	Theory	Experiment	Theory	Experiment	Theory	Experiment
V_0 (Å ³)	177.22(18) ^a	175.63(3) ^d	166.5(3) ^a		327.2(2) ^a	321.48 ^f	302.9(4) ^a	297.14 ^f
	178 ^b		167.0 ^b		302 ^e		302 ^e	
	174.9 ^c		160.3 ^c					
K_0 (GPa)	189(2) ^a	198(2) ^d	177(4) ^a		176.3(15) ^a		164(4) ^a	
	191 ^b		148 ^b		197 ^c			
	187.6 ^c		202.1 ^c					
K'	4.10(3) ^a	4.6(3) ^d	4.20(14) ^a		4.20(3) ^a		3.5(1) ^a	
	4.5 ^b		7.8 ^b					
	4.19 ^c		4.22 ^c					
Stability Range (GPa)	0 to 26.9 ^a	0 to 36 ^d	26.9 to >80 ^a		0 to 5.1 ^a	0 to ~6 ^g	5.1 to 11.2 ^a	~6 to ~10 ^g
	0 to 26.5 ^b		26.5 to ~80 ^b					
	0 to 27.06 ^c							

Parameter	UO ₂ (<i>Fm3m</i>)		UO ₂ (<i>Pnma</i>)		USiO ₄ (<i>I4₁/amd</i>)		USiO ₄ (<i>I4₁/a</i>)	
	Uraninite		—		Coffinite		—	
	Theory	Experiment	Theory	Experiment	Theory	Experiment	Theory	Experiment
V_0 (Å ³)	167.303 ^a	163.95(4) ^d	158.208 ^a		312.662 ^a	306.25(6) ⁱ	277.973 ^a	273.0 ⁱ
	161 ^h	158.9(5) ⁱ	152.3 ^h		284 ^e	305.58(2) ^j	270 ^e	
					306.21 ^j		271.39 ^j	
K_0 (GPa)	176.878 ^a	207(2) ^d	151.381 ^a		162.445 ^a	188(4) ⁱ	189.599 ^a	274(16) ⁱ
	208.3 ^h		192.5 ^h		217 ^e	181(5) ^j	212(1) ^j	195(6) ^j
					190(1) ^j			
K'	3.65021 ^a	4.5(4) ^d	4.77824 ^a		4 ^{a*}	4 ^{i*}	4 ^{a*}	
Stability Range (GPa)	0 to 29.2 ^a	0 to ~40 ^d	29.2 to >80 ^a		0 to 6.4 ^a	0 to 14–17 ⁱ	6.4 to 51.7 ^a	14–17 up to 45 ⁱ
	0 to 38 ^h		38 to ~80 ^h		0 to 6 ^e	0 to ~15 ^j	~15 to >35 ^j	
					0 to ~15 ^j			

Notes: ^aThis study, ^bWang et al., 2010, ^cQiang et al., 2014, ^dIdiri et al., 2004, ^eBose et al., 2009, ^fTayler and Ewing, 1978, ^gLiu 1982, ^hGeng et al., 2007, ⁱZhang et al., 2009, ^jBauer et al., 2014
*Fixed to 4.

Table 1. Equations of states of actinide oxide and silicate phases, where V_0 is the zero pressure volume, K_0 is the zero-pressure bulk modulus, and K' is the pressure derivative of the bulk modulus. No experimental compression equations of state have been measured for the *Pnma* phases of AO_2 or huttonite, and no ab initio equations of state have been calculated for huttonite.

FIGURES

Figure 1.

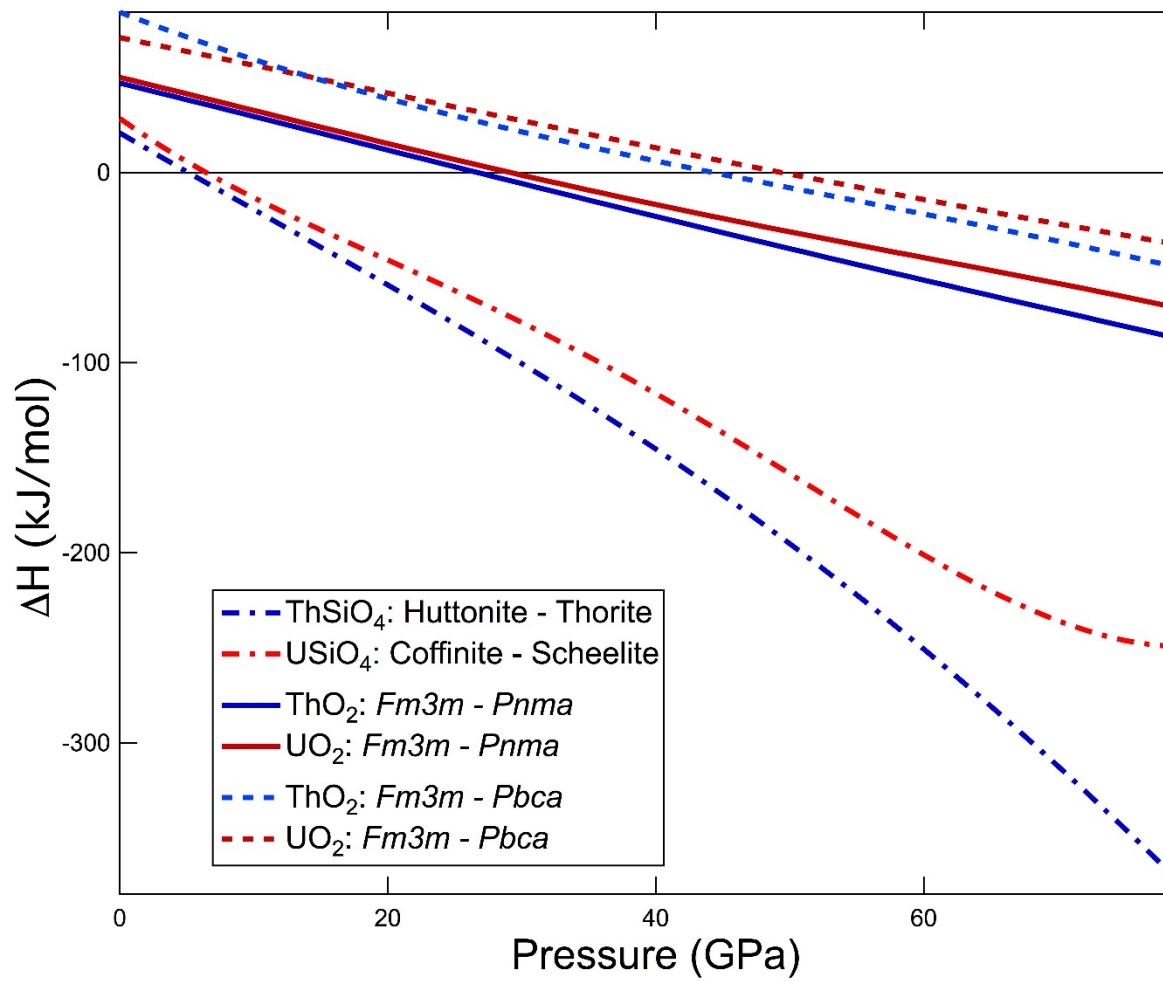


Figure 2.

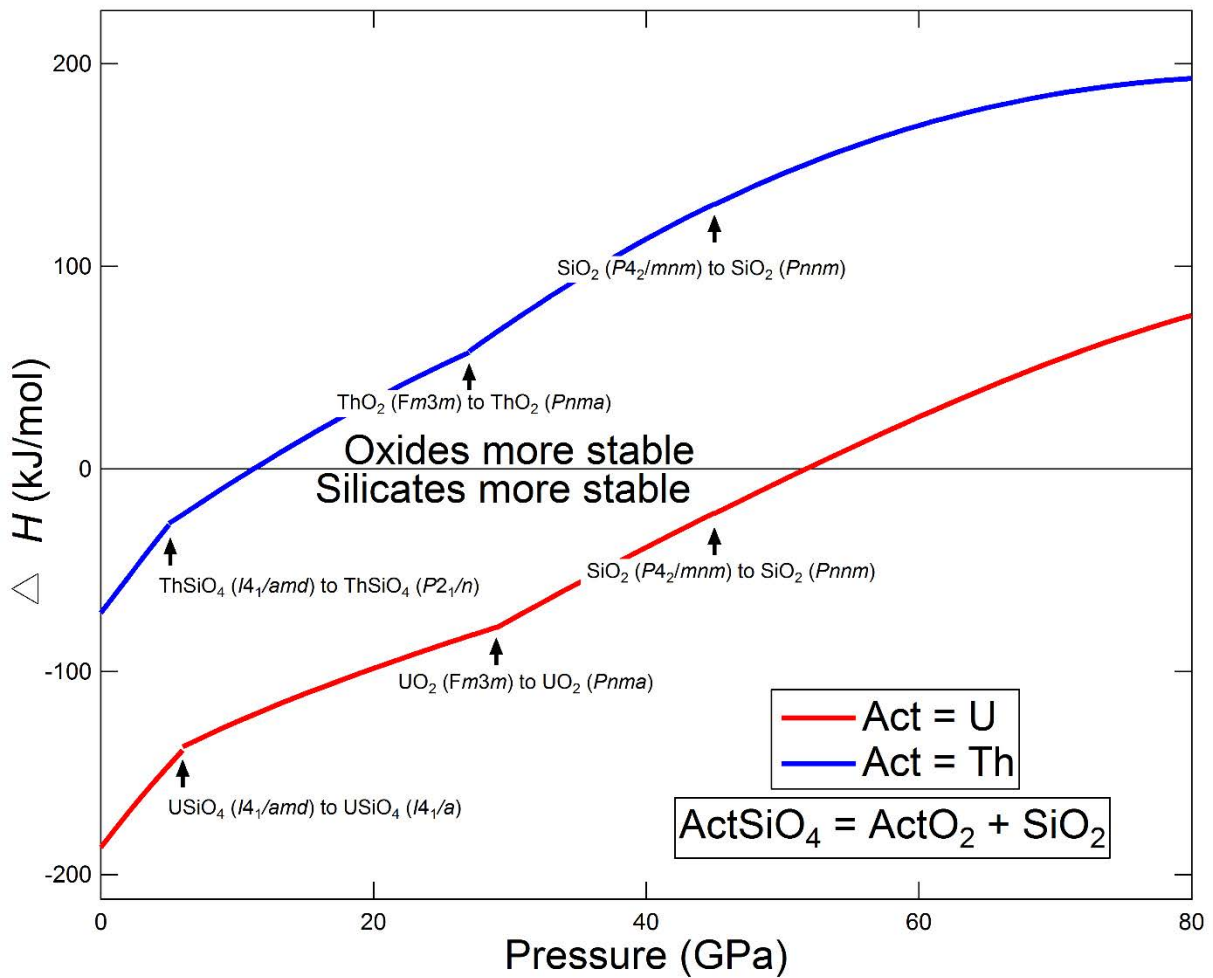


Figure 3.

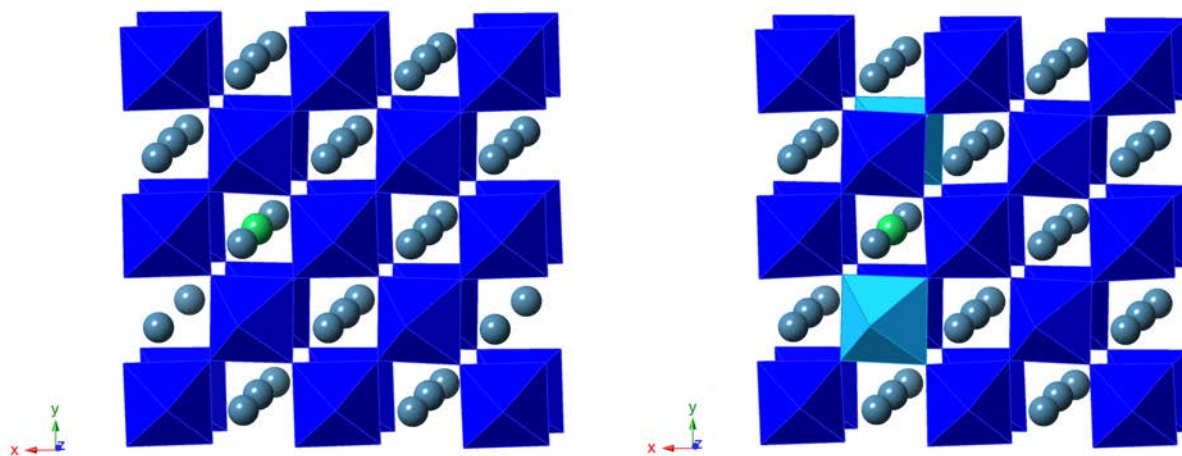


Figure 4.

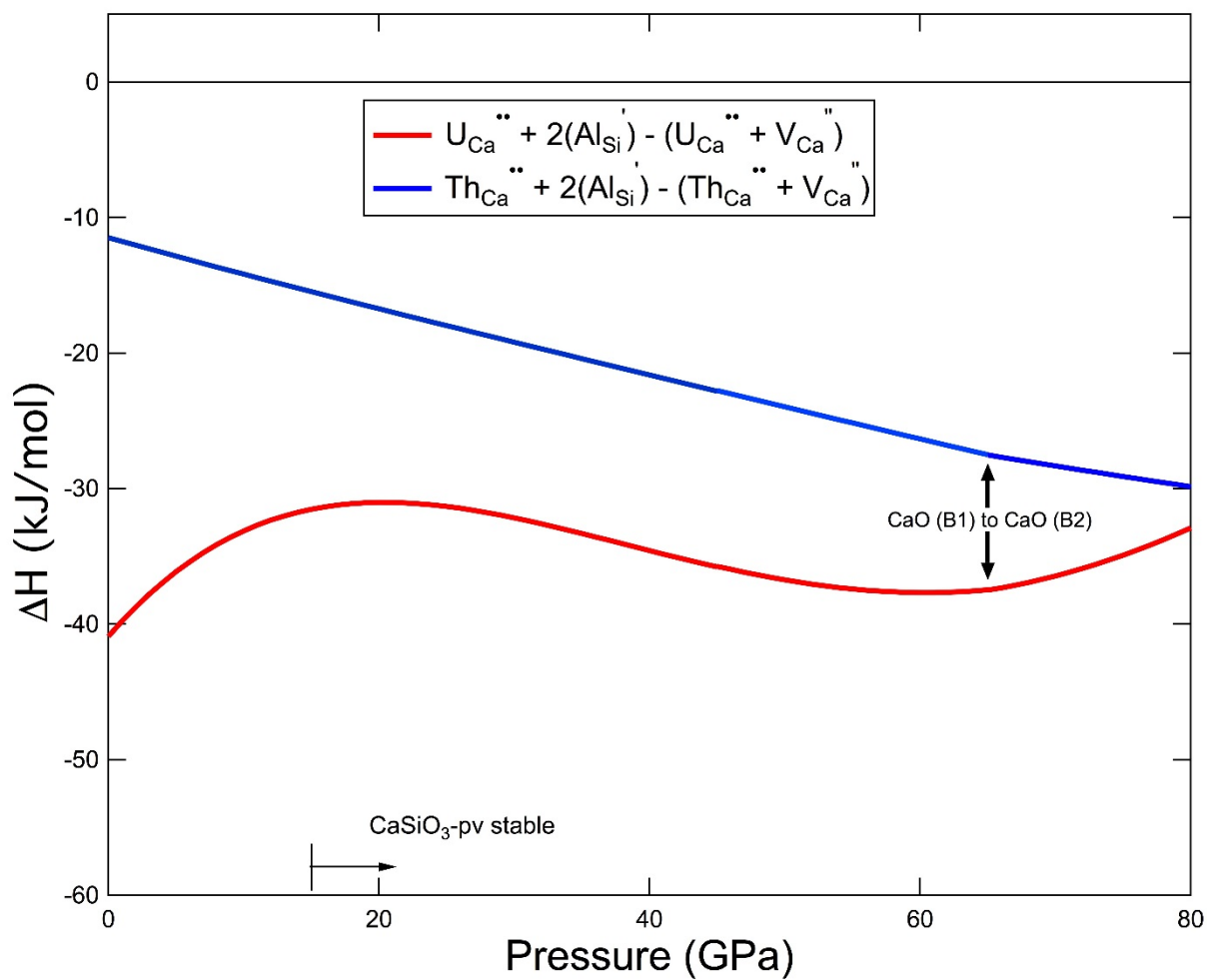


Figure 5.

